

High-resolution photoelectron imaging spectroscopy of cryogenically cooled Fe4O⁻ and Fe5O⁻

Marissa L. Weichman, Jessalyn A. DeVine, and Daniel M. Neumark

Citation: *The Journal of Chemical Physics* **145**, 054302 (2016); doi: 10.1063/1.4960176

View online: <http://dx.doi.org/10.1063/1.4960176>

View Table of Contents: <http://scitation.aip.org/content/aip/journal/jcp/145/5?ver=pdfcov>

Published by the [AIP Publishing](#)

Articles you may be interested in

[Photoelectron imaging and photodissociation of ozonide in O₃ - · \(O₂\)_n \(n = 1-4\) clusters](#)

J. Chem. Phys. **142**, 124305 (2015); 10.1063/1.4916048

[Slow photoelectron velocity-map imaging spectroscopy of the Fe₃O⁻ and Co₃O⁻ anions](#)

J. Chem. Phys. **141**, 174307 (2014); 10.1063/1.4900646

[High-resolution photoelectron imaging of cold C₆₀ - anions and accurate determination of the electron affinity of C₆₀](#)

J. Chem. Phys. **140**, 224315 (2014); 10.1063/1.4881421

[Resonant photoelectron spectroscopy of Au₂ - via a Feshbach state using high-resolution photoelectron imaging](#)

J. Chem. Phys. **139**, 194306 (2013); 10.1063/1.4830408

[Addition of water to Al₅O₄ - determined by anion photoelectron spectroscopy and quantum chemical calculations](#)

J. Chem. Phys. **122**, 014313 (2005); 10.1063/1.1828043

Ready, set, simulate.

REGISTER FOR THE COMSOL CONFERENCE >>



High-resolution photoelectron imaging spectroscopy of cryogenically cooled Fe_4O^- and Fe_5O^-

Marissa L. Weichman,¹ Jessalyn A. DeVine,¹ and Daniel M. Neumark^{1,2,a)}

¹Department of Chemistry, University of California, Berkeley, California 94720, USA

²Chemical Sciences Division, Lawrence Berkeley National Laboratory, Berkeley, California 94720, USA

(Received 10 June 2016; accepted 20 July 2016; published online 4 August 2016)

We report high-resolution photodetachment spectra of the cryogenically cooled iron monoxide clusters Fe_4O^- and Fe_5O^- obtained with slow photoelectron velocity-map imaging (cryo-SEVI). Well-resolved vibrational progressions are observed in both sets of spectra, and transitions to low-lying excited states of both species are seen. In order to identify the structural isomers, electronic states, and vibrational modes that contribute to the cryo-SEVI spectra of these clusters, experimental results are compared with density functional theory calculations and Franck-Condon simulations. The main bands observed in the SEVI spectra are assigned to the $^{15}A_2 \leftarrow ^{16}B_2$ photodetachment transition of Fe_4O^- and the $^{17}A' \leftarrow ^{18}A''$ photodetachment transition of Fe_5O^- . We report electron affinities of 1.6980(3) eV for Fe_4O and 1.8616(3) eV for Fe_5O , although there is some uncertainty as to whether the $^{15}A_2$ state is the true ground state of Fe_4O . The iron atoms have a distorted tetrahedral geometry in $\text{Fe}_4\text{O}^{0/-}$ and a distorted trigonal-bipyramidal arrangement in $\text{Fe}_5\text{O}^{0/-}$. For both neutral and anionic species, the oxygen atom preferably binds in a μ_2 -oxo configuration along the cluster edge. This finding is in contrast to prior predictions that $\text{Fe}_5\text{O}^{0/-}$ exhibits a μ_3 face-bound structure. *Published by AIP Publishing.* [<http://dx.doi.org/10.1063/1.4960176>]

I. INTRODUCTION

Bulk and nano-structured iron oxide materials have varied uses as catalysts for CO oxidation,^{1,2} the water-gas shift reaction,^{3,4} Fischer-Tropsch synthesis,⁵ and hydrocarbon dehydrogenation⁶ and oxidation.⁷ They also serve as supports for other catalysts.⁸ Interest in the reactivity and chemistry of these materials has spurred investigation of the properties and behavior of molecular-scale iron oxide clusters. Gas-phase clusters can provide insight into the local geometry and behavior of heterogeneous catalysts.⁹ The unusual structural motifs and distinct stoichiometry of small clusters can provide useful models for reactive point defects on surfaces.^{10,11} Small clusters are also accessible to theoretical as well as experimental study.¹² The ability to mass-select charged clusters allows for experimental investigation of the impact of size and stoichiometry on cluster properties and reactivity.^{13–15} It has also been suggested that some clusters demonstrate enhanced reactivity relative to the bulk, due to the wider range of stable stoichiometries, higher densities of reactive sites, and lowered barriers to isomerization.¹⁶

Spectroscopic and theoretical characterization of the geometries and electronic states of metal oxide clusters is essential for interpretation of their behavior and reactivity¹⁷ and, by extension, for understanding the behavior and reactivity of catalytic sites in the bulk. In the current work, we report vibrationally resolved photodetachment spectra of the iron monoxide clusters Fe_4O^- and Fe_5O^- via slow electron velocity-map imaging of cryogenically cold anions

(cryo-SEVI). This technique previously yielded detailed structures of the smaller transition metal monoxide clusters Fe_3O^- and Co_3O^- ,¹⁸ and was used to identify and order the energies of close-lying structural isomers in Ti_2O_4^- and Zr_2O_4^- .¹⁹ We demonstrate here that more complex polymetal clusters are also accessible to characterization with cryo-SEVI, and that, with the aid of density functional theory (DFT) calculations, we can confidently assign their geometric, vibrational, and electronic structure, despite many low-lying spin states and structural isomers.

Polymetal iron oxide clusters with varying composition and charge states have been studied previously with a number of experimental methods. In the gas phase, the mass spectra of iron oxide clusters formed by laser ablation have been characterized^{20–23} as have their photodissociation²⁴ and collision-induced dissociation²⁵ products. Reactions of gas-phase iron oxide clusters with N_2 ,²⁶ methanol,^{27,28} and CO ^{29–32} have been investigated. Spectroscopic characterization is more scarce, though some iron oxide clusters have been studied with anion photoelectron spectroscopy (PES)³³ and matrix isolation infrared spectroscopy.³⁴ There has also been theoretical investigation of the structures of some larger iron oxide species.^{35–38}

Among the iron monoxide clusters $\text{Fe}_n\text{O}^{0/-}$, the diatomic $\text{FeO}^{0/-}$ species are by far the most well-studied.^{39–44} Spectroscopic work on larger iron monoxide clusters is limited to photoelectron spectroscopy. Fe_nO^- clusters have been studied with conventional anion PES at fairly low resolution for n up to 16,⁴⁵ and at higher resolution for $n = 2-6$.⁴⁶ These studies did not resolve any vibrational structure in the spectra of Fe_4O^- and Fe_5O^- , though the authors observed sharp electronic bands, suggesting largely vertical transitions

^{a)}Author to whom correspondence should be addressed. Electronic mail: dneumark@berkeley.edu.

that result in little vibrational excitation of the neutral clusters upon photodetachment. Stern-Gerlach magnetic deflection experiments on neutral Fe_nO for $n = 2-7$ showed that these monoxide clusters are ferromagnetic, with magnetic moments that exceed those of the corresponding bare Fe_n clusters.⁴⁷

The theoretical literature suggests that the geometries and the electronic spin states of small $\text{Fe}_n\text{O}^{0/-}$ clusters are similar to those of the bare iron clusters $\text{Fe}_n^{0/-}$,⁴⁸ with the oxygen atom adsorbed on the cluster surface.^{18,45,46,49,50} The oxygen can be accommodated in an edge-bound two-fold coordinated μ_2 site, or a face-bound, three-fold coordinated μ_3 site; structures suggested by the literature for $\text{Fe}_4\text{O}^{0/-}$ and $\text{Fe}_5\text{O}^{0/-}$ are shown in Fig. 1. Prior work is in agreement that the most stable structures for $\text{Fe}_4\text{O}^{0/-}$ have the O atom at the μ_2 site (Fig. 1(a)).^{45,46,49,50} Gutsev *et al.*⁴⁶ report the most thorough DFT study on small $\text{Fe}_n\text{O}^{0/-}$ clusters in the literature, using BPW91/6-311+G*, and find an anionic Fe_4O^- ground state with C_{2v} symmetry and $2S + 1 = 16$ spin multiplicity. A 13-tet C_{2v} -symmetric structure is identified as the Fe_4O ground state, though a 15-tet state with C_2 symmetry lies only 0.01 eV higher.

There is less agreement in the literature regarding the structures of $\text{Fe}_5\text{O}^{0/-}$, particularly whether the O atom is preferentially accommodated in the μ_2 or μ_3 site (Figs. 1(b) and 1(c)). Early work by Wang *et al.*⁴⁵ using a local-spin-density method found that the neutral Fe_5O cluster had a 17-tet ground state, and a μ_2 geometry 0.06 eV more stable than the μ_3 geometry. Shiroishi *et al.*⁴⁹ also report a μ_2 ground state geometry for Fe_5O using DFT methods. Gutsev *et al.*,⁴⁶ however, report only μ_3 geometries for $\text{Fe}_5\text{O}^{0/-}$. They find an 18-tet anion ground state, a 17-tet neutral ground state, and a 19-tet neutral excited state lying 0.12 eV above the 17-tet.

Using high-resolution photoelectron imaging of cryogenically cooled anions in conjunction with DFT calculations, we can gain insight into the electronic and vibrational structure of $\text{Fe}_4\text{O}^{0/-}$ and $\text{Fe}_5\text{O}^{0/-}$. The cryo-SEVI technique represents a significant improvement in resolution over conventional anion PES and is well-suited for the study of complex transition metal oxide clusters.^{18,19} Experimental energy resolution down to $\sim 1 \text{ cm}^{-1}$ allows for full vibrational resolution of photodetachment bands,^{47,48} compared to the more typical resolution of $> 100 \text{ cm}^{-1}$ in prior PES work. Spectral clarity is improved by the preparation of cryogenically cold anions, which eradicates vibrational hot bands and dramatically narrows the rotational envelopes of photodetachment features.

Our cryo-SEVI photodetachment spectra of Fe_4O^- and Fe_5O^- yield well-resolved vibrational structure from which we obtain fundamental vibrational frequencies for Fe_4O and

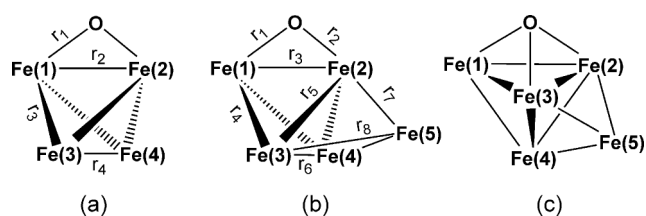


FIG. 1. Structures of (a) the C_{2v} -symmetric μ_2 structure of $\text{Fe}_4\text{O}^{0/-}$, (b) the C_s -symmetric μ_2 , and (c) C_1 -symmetric μ_3 structures of $\text{Fe}_5\text{O}^{0/-}$.

Fe_5O . Comparison to electronic structure calculations and Franck-Condon (FC) simulations is essential for interpretation of these results. $\text{Fe}_4\text{O}^{0/-}$ and $\text{Fe}_5\text{O}^{0/-}$ are found to take on structures with a μ_2 bridging oxo bound to iron atoms in a distorted tetrahedral configuration for Fe_4O and a distorted trigonal bipyramidal configuration for Fe_5O (Figs. 1(a) and 1(b)). We assign a $^{16}B_2$ ground state for Fe_4O^- , and observe a transition to the $^{15}A_2$ state of neutral Fe_4O , the lowest-energy state accessible with one-electron photodetachment. In Fe_5O^- , we report a transition from the $^{18}A''$ anion ground state to the neutral $^{17}A'$ ground state. For both clusters, we also observe photodetachment to a low-lying excited electronic state.

II. EXPERIMENTAL METHODS

The cryo-SEVI method has been described in detail elsewhere.⁵¹⁻⁵³ Briefly, iron oxide clusters are generated with a laser ablation source. They are trapped and cryo-cooled, mass-selected, and then photodetached with tunable light. The electron kinetic energy (eKE) distribution of the resulting photoelectrons is measured with a velocity-map imaging (VMI) spectrometer. We operate with low VMI extraction voltages and at laser energies very close to transition thresholds, so the slow electrons are preferentially detected and magnified on the imaging detector, resulting in high energy resolution.

Fe_nO^- anions are prepared in a pulsed laser ablation source operating at 20 Hz. During each cycle, a 2-10 mJ pulse of 532 nm light from a frequency doubled Nd:YAG laser is focused onto a steel ablation target. The resulting plasma is quenched in a burst of helium buffer gas from a pulsed Even-Lavie solenoid valve.⁵⁴ The presence of trace oxygen in the buffer gas allows for formation of the desired iron oxide clusters. The anions then pass through a radiofrequency (RF) hexapole ion guide, are mass selected with a quadrupole mass filter, and are directed into a linear RF octopole ion trap. The ions are stored in the trap for 40 ms, during which time they undergo cooling via collisions with an 80:20 He/ H_2 buffer gas mixture held at 5 K. These conditions should maximize the population of the ions in their ground vibrational and electronic states; we have measured molecular ion temperatures as low as 10 K after extraction from the trap.⁵³

The clusters are extracted from the trap into an orthogonal Wiley-McLaren time-of-flight mass spectrometer.⁵⁵ The ion packet then reaches the VMI spectrometer and is photodetached with the output of an Nd:YAG-pumped tunable dye laser. The resulting photoelectrons are focused with a VMI electrostatic lens⁵⁶ onto a detector consisting of two chevron-stacked micro-channel plates (MCPs) coupled to a phosphor screen.⁵⁷ The new design of our VMI lens was reported recently.⁵⁸ Events on the screen are recorded with a CCD camera, and event counting software is used to identify the single electron events and compute their centroids in real time during data acquisition.⁵⁹ Centroids are binned into a sufficiently fine grid to ensure the bin size does not limit the instrumental resolution of the spectrometer. A single VMI image is produced by accumulating the centroids of electron spots over several thousand experimental cycles.

The maximum-entropy velocity Legendre reconstruction method⁶⁰ is used to reconstruct the radial and angular electron distributions from an accumulated image. We calibrate the photoelectron velocity and hence the electron kinetic energy (eKE) as a function of radial displacement from the center of the reconstructed image using SEVI images of well-characterized photodetachment transitions of atomic O^- .⁶¹ As the eKE is a function of photodetachment laser energy ($h\nu$), we report SEVI spectra in electron binding energy (eBE), given by $eBE = h\nu - eKE$.

VMI spectrometers yield the best resolution for low-eKE transitions.⁶² We make measurements at discrete photodetachment energies tuned just above the spectral features of interest in order to image each transition close to threshold. These windows are then spliced together to create a composite high-resolution spectrum, as discussed previously.⁶³ The intensity of each high-resolution window is scaled to match its intensity in an overview spectrum taken at a photon energy well above the band of interest to minimize threshold effects that may distort the relative peak intensities.

III. EXPERIMENTAL RESULTS

The cryo-SEVI spectra of Fe_4O^- and Fe_5O^- are presented in Figs. 2 and 3, respectively. Low-resolution overview traces are plotted in blue, with high-resolution composite traces plotted in black. The photodetachment bands of the two species are similar in appearance, with strong vibrational origins (peak A in Figs. 2 and 3) and relatively weak structure continuing for about 1000 cm^{-1} . Franck-Condon simulations discussed below demonstrate that this weak structure (peaks B-H in Fig. 2 and B-I in Fig. 3) corresponds to transitions to vibrationally excited states of neutral Fe_4O and Fe_5O . Both SEVI spectra also demonstrate an additional feature at higher eBE (peak X in Figs. 2 and 3). Due to the separation in energy between peak X and the main band in each spectrum, peak X is assigned as photodetachment to a second neutral electronic state. Peak positions and assignments for the spectral features in the cryo-SEVI spectra of Fe_4O^- and Fe_5O^- are given in Tables I and II, respectively. Peak positions represent the center of a Gaussian fit. Typical peak widths in the composite traces are 6 cm^{-1} fwhm.

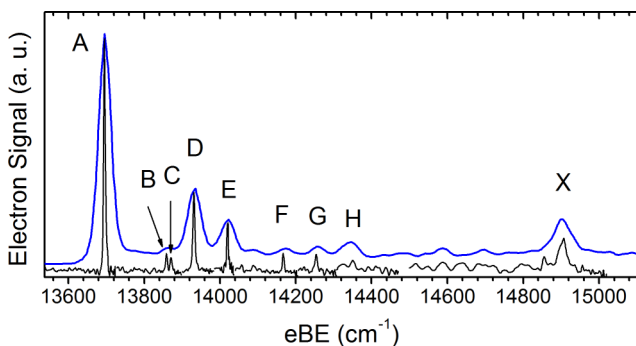


FIG. 2. Cryo-SEVI spectra of Fe_4O^- . The blue trace is an overview spectrum taken at $16\,180\text{ cm}^{-1}$ while the black segments are high-resolution portions of scans taken at lower photon energies.

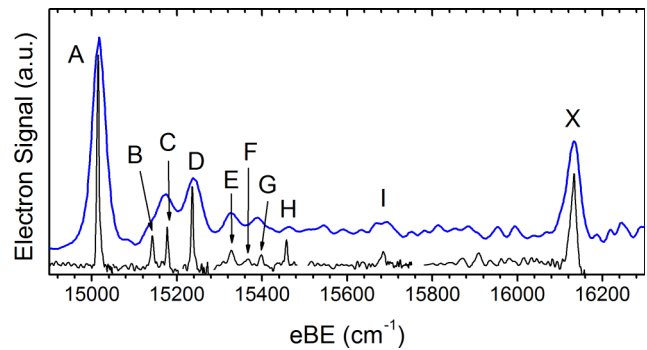


FIG. 3. Cryo-SEVI spectra of Fe_5O^- . The blue trace is an overview spectrum taken at $16\,665\text{ cm}^{-1}$ while the black segments are high-resolution portions of scans taken at lower photon energies.

We can also extract information on the photoelectron angular distribution (PAD) from the SEVI images. For one-photon photodetachment with linearly polarized light, the PAD is given by⁶⁴

$$\frac{d\sigma}{d\Omega} = \frac{\sigma_{tot}}{4\pi} [1 + \beta P_2(\cos\theta)]. \quad (1)$$

Here θ is the angle relative to the polarization axis of the laser, P_2 is the second order Legendre polynomial, and β is the anisotropy parameter which varies between -1 and $+2$ for PADs aligned perpendicular and parallel to the laser polarization, respectively.

In the SEVI spectra of Fe_4O^- , peaks A-H demonstrate weakly-negative-to-isotropic anisotropy parameters ($-0.2 < \beta < -0.1$) close to threshold and weakly positive anisotropy parameters ($\beta \sim 0.25$) by 2000 cm^{-1} above threshold. The PAD of peak X is isotropic at small eKE, and grows more negative farther above threshold. For the Fe_5O^- spectra, peaks A-I have consistently negative positive anisotropy parameters starting at $\beta \sim -0.2$ near threshold, and decreasing to $\beta \sim -0.35$ by 1000 cm^{-1} above threshold. The PAD of peak X, on the other hand, remains isotropic over the range of eKE measured here. Hence, for both anions, the PADs further support the assignment of peak X to a different electronic band than the features at lower eBE.

TABLE I. Peak positions (cm^{-1}), offsets from the origin (cm^{-1}), and assignments for the SEVI spectra of Fe_4O^- given in Fig. 2. Uncertainties represent one standard deviation of a Gaussian fit to the experimentally observed peak.

Peak	Position	Offset	Assignment
A	13 695(2)	0	0_0^0
B	13 859(2)	163	5_0^2
C	13 871(3)	175	4_0^1
D	13 931(2)	236	3_0^1
E	14 020(2)	325	2_0^1
F	14 167(2)	472	3_0^2
G	14 254(3)	558	2_0^{131}
H	14 350(6)	654	2_0^2
X	14 904(10)	1208	$\bar{A} 0_0^0$

TABLE II. Peak positions (cm^{-1}), offsets from the origin (cm^{-1}), and assignments for the SEVI spectra of Fe_5O^- given in Fig. 3. Uncertainties represent one standard deviation of a Gaussian fit to the experimentally observed peak.

Peak	Position	Offset	Assignment
A	15 015(3)	0	0_0^0
B	15 142(3)	128	8_0^1
C	15 177(3)	163	7_0^1
D	15 236(2)	221	5_0^1
E	15 328(5)	313	3_0^1
F	15 366(6)	351	$5_0^1 8_0^1$
G	15 398(4)	383	$5_0^1 7_0^1$
H	15 457(2)	443	5_0^2
I	15 684(4)	670	1_0^1
X	16 131(7)	1117	$\tilde{A} 0_0^0$

Over the range of photon energies used to obtain the SEVI spectrum of Fe_5O^- , we observe a background of electrons with an eKE distribution characteristic of thermionic emission.⁶⁵ A representative Fe_5O^- spectrum is presented in Fig. S1⁷⁴ demonstrating the contributions of both thermionic emission and direct detachment. Gutsev *et al.*⁴⁶ observed similar signatures of thermionic emission in the anion photoelectron spectra of Fe_5O^- . The thermionic emission signal increases in intensity relative to the direct detachment signal as the photon energy is increased. The SEVI traces taken at higher photon energies in Fig. 3 have therefore been baseline corrected to account for this background. Because we observe thermionic emission signal extending to higher eKE than the vibrational origin of the Fe_5O^- cluster, we ascribe at least some of this signal to weak two-photon absorption.

IV. THEORETICAL METHODS AND RESULTS

A. Electronic structure calculations

To aid in interpreting our spectra, we have carried out DFT calculations to identify the lowest-lying electronic states, optimized geometries, normal modes, and harmonic vibrational frequencies for the $\text{Fe}_4\text{O}^{0/-}$ and $\text{Fe}_5\text{O}^{0/-}$ clusters.

For $\text{Fe}_4\text{O}^{0/-}$, we focus on C_{2v} - and C_2 -symmetric μ_2 structures; our attempts to find a μ_3 structure for 16-tet Fe_4O^- also converged to the μ_2 structure. For $\text{Fe}_5\text{O}^{0/-}$, we searched extensively for μ_2 and μ_3 structures to attempt to resolve the discrepancies in the literature. Calculations were performed with the TPSS, BPW91, and BP86 density functionals in order to assure consistency across the results from each. The BPW91 and BP86 functionals have provided accurate comparisons for prior cryo-SEVI results on polymetal oxide clusters;^{18,19} the TPSS functional is also known to perform well for certain transition metal systems.⁶⁶ The 6-311+G* basis set was used for both Fe and O atoms with full treatment of all electrons.^{67,68} Calculations were carried out in Gaussian 09 with tight geometry optimization criteria and an ultrafine integration grid.⁶⁹

Figs. 4 and 5 show the calculated relative energies for low-lying states of $\text{Fe}_4\text{O}^{0/-}$ and $\text{Fe}_5\text{O}^{0/-}$, respectively. In

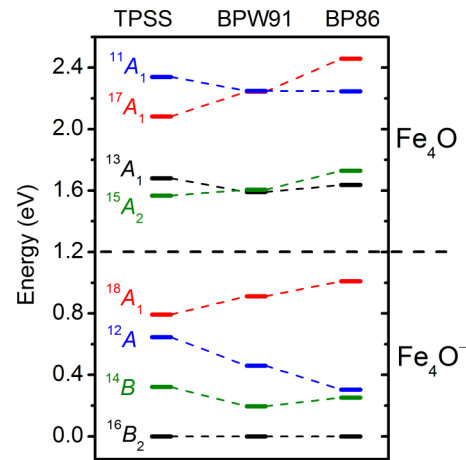


FIG. 4. Energy level diagram of low-lying $\text{Fe}_4\text{O}^{0/-}$ electronic spin states; symmetry labels are provided as found with TPSS. Energies are reported for the lowest energy optimized μ_2 structure for each spin state and are given relative to the anion ground state.

Fig. 4 we report only the energies for optimized μ_2 structures of $\text{Fe}_4\text{O}^{0/-}$ in various spin states, while in Fig. 5 we report the energies of the lowest-lying μ_2 and μ_3 structures for each spin state of $\text{Fe}_5\text{O}^{0/-}$. Full lists of energies, electronic state symmetries, and $\langle S^2 \rangle$ values for all states are given in Tables S1 and S2 in the supplementary material.⁷⁴ The values of $\langle S^2 \rangle$ generally fall very close to the expected result of $S(S+1)$, indicating little spin contamination in the DFT calculations. The supplementary material also contains information on additional higher-lying geometries found for some spin states. Optimized Cartesian coordinates and harmonic vibrational frequencies are reported for all states in Tables S3-S8 and Tables S9-S11,⁷⁴ respectively.

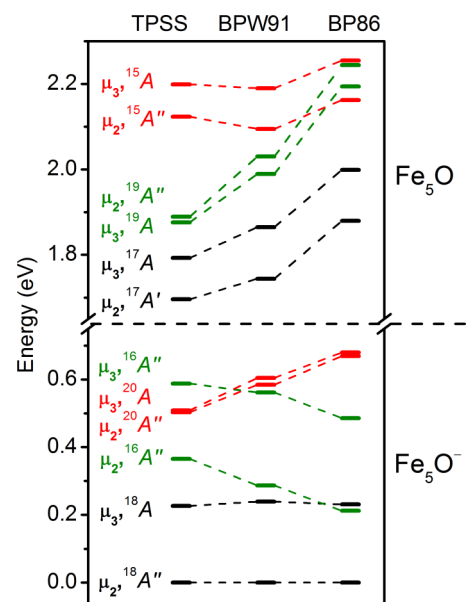


FIG. 5. Energy level diagram of low-lying $\text{Fe}_5\text{O}^{0/-}$ electronic spin states; symmetry labels are provided as found with TPSS. Energies are reported for the lowest energy optimized μ_2 and μ_3 structures for each spin state and are given relative to the anion ground state.

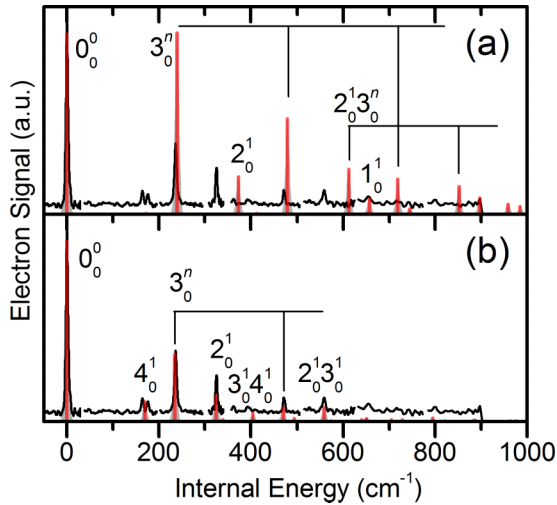


FIG. 6. (a) FC simulation of the $^{15}A_2 \leftarrow ^{16}B_2$ transition of $Fe_4O^{0/-}$ with TPSS/6-311+G* and (b) FC simulation after fitting the simulation parameters to a SEVI overview trace. Simulations are plotted as stick spectra (red) and after convolution with a 10 cm^{-1} fwhm Gaussian line shape function (grey), and compared to the high-resolution SEVI traces (black).

B. Franck-Condon simulations

Franck-Condon simulations were carried out at 0 K with the FCFGAUS and PESCAL programs,^{70,71} using the harmonic approximation with Duschinsky mixing of totally symmetric modes.⁷² FC simulations using TPSS/6-311+G* geometries and frequencies are reported in Fig. 6(a) for the $^{15}A_2 \leftarrow ^{16}B_2$ photodetachment transition of $Fe_4O^{0/-}$, and in Fig. 7(a) for the $^{17}A' \leftarrow ^{18}A''$ photodetachment transition between μ_2 structures of $Fe_5O^{0/-}$; these are the lowest energy photodetachment transitions from the calculated anion ground states. In both cases, they are plotted against high-resolution experimental spectra (black). FC simulations

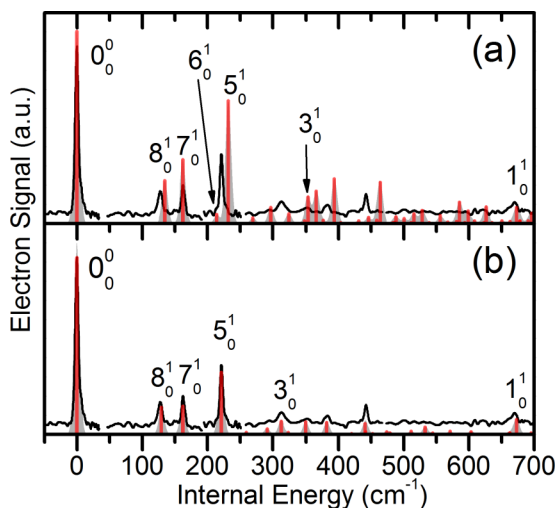


FIG. 7. (a) FC simulation of the $^{17}A' \leftarrow ^{18}A''$ transition between μ_2 structures of $Fe_5O^{0/-}$ with TPSS/6-311+G* and (b) FC simulation after fitting the simulation parameters to a SEVI overview trace. Simulations are plotted as stick spectra (red) and after convolution with a 10 cm^{-1} fwhm Gaussian line shape function (grey), and compared to the high-resolution SEVI traces (black).

TABLE III. Parameters for the TPSS/6-311+G* FC simulation of $Fe_4O^{0/-}$ photodetachment and fit to the SEVI spectrum of $Fe_4O^{0/-}$ shown in Fig. 6. Parameters optimized in the fitting include the frequencies ω_n of the totally symmetric modes of neutral Fe_4O , and displacements ΔQ_n along these modes between the anion and neutral geometries, given here in the normal mode basis of the anion. Also reported are the anion and neutral DFT bond lengths and neutral bond lengths after displacement fitting, if the anion geometry is kept fixed. Bond labels are given in Fig. 1(a).

Parameter	TPSS/6-311+G*		After fit
	$^{16}B_2$	$^{15}A_2$	$^{15}A_2$
$\omega_1 \text{ (cm}^{-1}\text{)}$	633	657	652
$\omega_2 \text{ (cm}^{-1}\text{)}$	352	373	324
$\omega_3 \text{ (cm}^{-1}\text{)}$	226	240	235
$\omega_4 \text{ (cm}^{-1}\text{)}$	160	172	170
$\Delta Q_1 \text{ (amu}^{1/2} \text{ \AA)}$...	-0.091	-0.038
$\Delta Q_2 \text{ (amu}^{1/2} \text{ \AA)}$...	-0.109	-0.111
$\Delta Q_3 \text{ (amu}^{1/2} \text{ \AA)}$...	-0.587	-0.359
$\Delta Q_4 \text{ (amu}^{1/2} \text{ \AA)}$...	-0.073	-0.239
$r_1 \text{ (\AA)}$	1.835	1.816	1.827
$r_2 \text{ (\AA)}$	2.414	2.466	2.462
$r_3 \text{ (\AA)}$	2.356	2.355	2.343
$r_4 \text{ (\AA)}$	2.279	2.183	2.221

carried out with BPW91 and BP86 yielded essentially identical results.

Since agreement between the experimental and simulated spectra in Figs. 6(a) and 7(a) is far from perfect, we also

TABLE IV. Parameters for the TPSS/6-311+G* FC simulation of $Fe_5O^{0/-}$ photodetachment and fit to the SEVI spectrum of $Fe_5O^{0/-}$ shown in Fig. 7. Parameters optimized in the fitting include the frequencies ω_n of the totally symmetric modes of neutral Fe_5O , and displacements ΔQ_n along these modes between the anion and neutral geometries, given here in the normal mode basis of the anion. Also reported are the anion and neutral DFT bond lengths and neutral bond lengths after displacement fitting, if the anion geometry is kept fixed. Bond labels are given in Fig. 1(b).

Parameter	TPSS/6-311+G*		After fit
	$^{18}A''$	$^{17}A'$	$^{17}A'$
$\omega_1 \text{ (cm}^{-1}\text{)}$	646	674	...
$\omega_3 \text{ (cm}^{-1}\text{)}$	338	354	313
$\omega_5 \text{ (cm}^{-1}\text{)}$	225	232	221
$\omega_6 \text{ (cm}^{-1}\text{)}$	213	214	214
$\omega_7 \text{ (cm}^{-1}\text{)}$	167	162	162
$\omega_8 \text{ (cm}^{-1}\text{)}$	128	135	130
$\Delta Q_1 \text{ (amu}^{1/2} \text{ \AA)}$...	-0.091	...
$\Delta Q_3 \text{ (amu}^{1/2} \text{ \AA)}$...	-0.094	-0.070
$\Delta Q_5 \text{ (amu}^{1/2} \text{ \AA)}$...	-0.363	-0.281
$\Delta Q_6 \text{ (amu}^{1/2} \text{ \AA)}$...	-0.156	-0.027
$\Delta Q_7 \text{ (amu}^{1/2} \text{ \AA)}$...	0.383	0.258
$\Delta Q_8 \text{ (amu}^{1/2} \text{ \AA)}$...	-0.489	-0.385
$r_1 \text{ (\AA)}$	1.811	1.792	1.802
$r_2 \text{ (\AA)}$	1.848	1.825	1.826
$r_3 \text{ (\AA)}$	2.332	2.347	2.339
$r_4 \text{ (\AA)}$	2.381	2.383	2.394
$r_5 \text{ (\AA)}$	2.435	2.434	2.435
$r_6 \text{ (\AA)}$	2.383	2.275	2.303
$r_7 \text{ (\AA)}$	2.355	2.360	2.361
$r_8 \text{ (\AA)}$	2.346	2.366	2.348

used PESCAL to perform nonlinear least-squares fits of the FC simulations to overview the SEVI spectra of Fe_4O^- and Fe_5O^- . Fitting parameters included the frequencies of totally symmetric FC active neutral vibrational modes, as well as displacements between the anion and neutral geometries along these modes. The frequency and displacement of the ν_1 mode of $\text{Fe}_5\text{O}^{0/-}$ were not varied during fitting, because the trace that proved best for fitting most of the band was taken at too low a photon energy to include the ν_1 fundamental. The eBE of the vibrational origin, the overall band intensity, and the width of the stick spectrum Gaussian convolution were also allowed to vary in the fitting routine for both clusters. Simulations fitted to the experimental traces are plotted in Figs. 6(b) and 7(b). Relevant parameters for the simulations and fits are summarized in Tables III and IV for Fe_4O^- and Fe_5O^- , respectively.

V. DISCUSSION

A. Structural isomers and electronic states

For $\text{Fe}_4\text{O}^{0/-}$, the energetics and μ_2 -oxo optimized geometries found here largely reproduce the results reported by Gutsev *et al.*⁴⁶ With all three functionals, we find a C_{2v} -symmetric $^{16}B_2$ ground state anion. A C_2 -symmetric ^{14}B state lies close above; this state lies slightly lower in energy than the 14-tet C_{2v} structure reported by Gutsev *et al.* The C_{2v} -symmetric 12-tet and 18-tet states lie correspondingly higher in energy. The three functionals used here agree on this state ordering, though for the 12-tet TPSS finds a C_2 -symmetric structure rather than the C_{2v} structures found with BPW91 and BP86.

For neutral Fe_4O , our calculations reproduce the two lowest energy, nearly degenerate C_{2v} -symmetric $^{13}A_1$ and C_2 -symmetric ^{15}A states identified by Gutsev *et al.*,⁴⁶ though the relative ordering of these states is uncertain. Additionally, there is a C_{2v} transition state for the 15-tet that lies only 12-50 cm^{-1} above the C_2 structure, depending on the functional. This structure corresponds to a barrier between the two equivalent C_2 structures that is either comparable to or submerged below vibrational zero-point energy. We therefore consider the neutral 15-tet to have C_{2v} symmetry with a shallow double-well potential along the a_2 -symmetric ν_5 normal coordinate. This anharmonic vibrational potential is discussed in more detail in Section V B.

Our calculations find that for neutral Fe_4O , the 11-tet state and 17-tet states lie considerably higher in energy and are nearly degenerate with one another. As was the case for the 15-tet, Gutsev *et al.*⁴⁶ report a C_2 structure for the 11-tet, while we find this state has functionally C_{2v} symmetry.

Regardless of the exact ordering of the Fe_4O neutral states, since the $^{16}B_2$ state is widely agreed upon as the anion ground state, one electron photodetachment can only access neutral 15-tet and 17-tet states. The assignment for the main photodetachment band in the Fe_4O^- SEVI spectrum is therefore $^{15}A_2 \leftarrow ^{16}B_2$, corresponding to the detachment of an electron from the highest-lying molecular orbital (HOMO) of the anion with α spin (visualized in Fig. 8(a)). If we take the Fe_4O $^{15}A_2$ state as the neutral ground state, in agreement

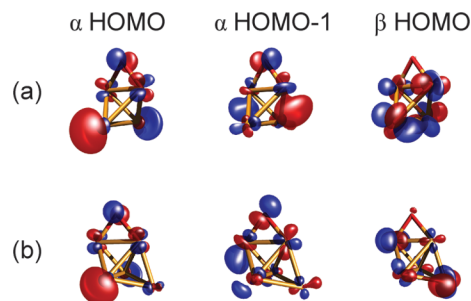


FIG. 8. Relevant high-lying molecular orbitals of (a) Fe_4O^- and (b) Fe_5O^- .

with the TPSS results, then the vibrational origin of the main photodetachment band in Fig. 2 directly yields the electron affinity (EA) of Fe_4O . However, the Fe_4O $^{13}A_1$ state is predicted to lie nearly degenerate in energy with the $^{15}A_2$ state and cannot be observed in our experiment. We therefore cannot unambiguously rule out the 13-tet as the ground state of Fe_4O .

Our calculations for $\text{Fe}_5\text{O}^{0/-}$ demonstrate a more significant departure from the work of Gutsev *et al.*,⁴⁶ who report only μ_3 geometries for these clusters. While we can largely reproduce their results, we also identify μ_2 geometries that are lower in energy than their μ_3 counterparts for most $\text{Fe}_5\text{O}^{0/-}$ spin states. Only the 19-tet neutral has a μ_3 structure more stable than the μ_2 structure, and the 20-tet anion has μ_2 and μ_3 structures comparable in energy. In some cases, we also find alternate μ_3 geometries that are lower or comparable in energy to those reported by Gutsev *et al.* All of these states are detailed in the supplementary material.⁷⁴

For Fe_5O^- , all three functionals find an $^{18}A''$ anion ground state with a C_s -symmetric μ_2 geometry. This state is consistently 0.23-0.24 eV lower in energy than the most stable 18-tet μ_3 structure identified by Gutsev *et al.*⁴⁶ The 16-tet and 20-tet μ_2 structures lie respectively higher in energy and are found to be C_1 -symmetric with BPW91 and BP86, but have higher C_s symmetry with the TPSS functional. For neutral Fe_5O , we find a $^{17}A'$ ground state with a C_s -symmetric μ_2 geometry that lies 0.10-0.12 eV below the μ_3 17-tet structure. 19-tet and 15-tet states lie higher in energy; the ordering of these states is reasonably consistent between functionals and with the work of Gutsev *et al.* With TPSS, we had difficulty optimizing the 15-tet μ_2 structure, and the state reported here has one small imaginary frequency.

With an $^{18}A''\mu_2$ -oxo ground state for Fe_5O^- , only 17-tet and 19-tet neutral states with μ_2 structures should be accessible through photodetachment. The main photodetachment band in the Fe_5O^- SEVI spectrum is therefore assigned to the $^{17}A' \leftarrow ^{18}A''$ transition, between the ground state C_s -symmetric μ_2 anion and neutral structures, and the vibrational origin of this band unambiguously yields the EA of Fe_5O . As was true for Fe_4O^- , this transition corresponds to detachment from the α HOMO (Fig. 8(b)).

In the experimental spectra in Figs. 2 and 3, peak A is the strong vibrational origin of each main photodetachment band. The eBE of each origin gives an EA of 1.6980(3) eV for Fe_4O and 1.8616(3) eV for Fe_5O , both of which fall within the range of calculated values (Table V). Note that our reported

TABLE V. All assigned states, state energies, and vibrational frequencies for $\text{Fe}_4\text{O}^{0/-}$ and $\text{Fe}_5\text{O}^{0/-}$. Calculated energies are corrected for vibrational zero-point energy.

		Expt.	TPSS	BPW91	BP86	
Fe_4O^-	$^{16}B_2$					
Fe_4O	$^{15}A_2$	EA, ^a eV	1.6980(3) ^b	1.5674 ^c	1.6054 ^c	1.7290 ^c
		ν_2 , cm^{-1}	325(2)	373	363	365
		ν_3 , cm^{-1}	236(2)	240	248	249
		ν_4 , cm^{-1}	175(3)	172	176	177
		$2\nu_5$, cm^{-1}	163(2)	149	125	127
	\tilde{A}	TE, ^d eV	0.1498(12)			
Fe_5O^-	$^{18}A''$					
Fe_5O	$^{17}A'$	EA, eV	1.8616(3)	1.6961	1.7440	1.8796
		ν_1 , cm^{-1}	670(4)	674	660	663
		ν_3 , cm^{-1}	313(5)	354	344	346
		ν_5 , cm^{-1}	221(2)	232	233	234
		ν_7 , cm^{-1}	163(3)	162	156	156
		ν_8 , cm^{-1}	128(3)	135	128	128
	\tilde{A}	TE, eV	0.1384(9)			

^aElectron affinity.

^bUncertainties represent one standard deviation of a Gaussian fit to the experimentally observed peak.

^cCalculated electron affinities for Fe_4O reflect the difference in energy between the $^{16}B_2$ anion and $^{15}A_2$ neutral states.

^dTerm energy.

and calculated EAs for Fe_4O assume that its ground state is the $^{15}A_2$ state, as mentioned above. For both species, we assign peak X as the vibrational origin of a second photodetachment band to a neutral excited state with an eBE of 1.8478(12) eV for Fe_4O and 2.0000(9) eV for Fe_5O . The photoelectron spectra reported previously by Gutsev *et al.*⁴⁶ demonstrated very sharp bands at vertical detachment energies of 1.70(2) eV and 1.85(2) eV for Fe_4O^- , and 1.87(2) eV and 2.00(2) eV for Fe_5O^- , in excellent agreement with our measurements of peaks A and X for both systems. The sharpness of the features observed by Gutsev *et al.* is also in accord with the intense vibrational origins and comparatively weak vibrational structure observed here.

For both clusters, the assignment of the neutral electronic excited state corresponding to peak X is somewhat speculative. This feature lies at a term energy of 0.1498(12) eV relative to the main photodetachment band for Fe_4O and at 0.1384(9) eV for Fe_5O . One-electron photodetachment from the $^{16}B_2$ state of Fe_4O^- can access both neutral 15-tet and 17-tet states, while 17-tet and 19-tet neutral states are similarly accessible from the $^{18}A''$ state of Fe_5O^- . For Fe_4O , the lowest-lying 17-tet state is calculated to lie 0.52-0.73 eV above the $^{15}A_2$ state (Table S1⁷⁴), considerably higher than what is observed experimentally. The lowest 19-tet state of neutral Fe_5O is calculated to lie at a term energy of 0.19-0.36 eV above the $^{17}A'$ ground state (Table S2⁷⁴), which is within DFT error of the experimental term energy of peak X. These high-spin neutral states are accessible from detachment of the β HOMOs (Fig. 8) of Fe_4O^- and Fe_5O^- . Another scenario for both species is that peak X represents a transition to an excited state with the same spin multiplicity as the main photodetachment band, corresponding to detachment from the anion α HOMO-1, also visualized in Fig. 8. While we are

unable to calculate the term energies of excited Fe_4O 15-tet and Fe_5O 17-tet states, it is worth noting that our experiment would be sensitive to the plethora of detachment transitions from α HOMO-*n* orbitals. The fact that we observe only two bands for each cluster in the energy window considered here suggests that these orbitals are spaced farther apart in energy than one might expect given the high electronic spin in these systems.

For $\text{Fe}_4\text{O}^{0/-}$, the photoelectron angular distributions of the main detachment band and of peak X are qualitatively consistent with the electronic state assignments discussed above. A model developed by Sanov and co-workers⁷³ can predict the near-threshold PAD upon photodetachment of a C_{2v} molecular anion. In the $^{15}A_2 \leftarrow ^{16}B_2$ photodetachment transition of Fe_4O^- , an electron is ejected from the b_1 -symmetric α HOMO. Within this model, this transition should yield a PAD aligned perpendicular to the laser polarization that grows isotropic at low eKE, as is reasonably consistent with the near-threshold behavior of peaks in the main photodetachment band. Detachment from the β HOMO and α HOMO-1 of Fe_4O^- , both with b_2 symmetry, yields the lowest 17-tet and first excited 15-tet states of Fe_4O . Within the Sanov model, ejection of an electron from a b_2 orbital also yields a perpendicular PAD that grows isotropic close to threshold. This PAD is consistent with that observed experimentally for peak X, and unfortunately does not aid in clarifying the excited band assignment.

The low symmetry C_s point group of $\text{Fe}_5\text{O}^{0/-}$ makes prediction of PADs more challenging than for $\text{Fe}_4\text{O}^{0/-}$. However, the a'' -symmetric Fe_5O^- α HOMO looks very similar to the b_1 -symmetric α HOMO of Fe_4O^- , with electron density largely in *s*-like antibonding orbitals on the Fe(3) and Fe(4) atoms, and very little participation of the additional Fe(-5) atom (atoms labeled in Fig. 1). It is therefore reasonable to expect that the main Fe_5O^- photodetachment band also has a PAD aligned perpendicular to the laser polarization axis that grows isotropic close to threshold, and indeed this is what is observed experimentally. The low-lying excited state (peak X) exhibits an isotropic PAD which does not allow us to distinguish between detachment from the β HOMO and α HOMO-1 of Fe_5O^- , both of which have a' symmetry.

B. Vibrational structure

We use calculated harmonic vibrational frequencies and simulated FC envelopes to assign the vibrational structure of the Fe_4O^- and Fe_5O^- SEVI spectra. The $\text{Fe}_4\text{O}^{0/-}$ clusters have four totally symmetric a_1 vibrational modes within the C_{2v} point group, while the C_s -symmetric $\text{Fe}_5\text{O}^{0/-}$ species have eight totally symmetric a' vibrational modes. These modes are shown schematically in Fig. S2.⁷⁴ The TPSS/6-311+G* frequencies for FC active modes and displacements along these modes for the $^{15}A_2 \leftarrow ^{16}B_2$ photodetachment transition of Fe_4O^- and the $^{17}A' \leftarrow ^{18}A''$ transition of Fe_5O^- are summarized in Tables III and IV. These calculated parameters yield the FC simulations shown in Figs. 6(a) and 7(a).

For Fe_4O^- , the FC simulation in Fig. 6(a) shows predominant excitation in mode ν_2 , some excitation in ν_3 , and weaker still activity in ν_1 . Qualitatively, moderate excitation

in a few modes matches the experimental spectrum; the largest discrepancies are the simulated overemphasis of FC intensity for the ν_3 progression, and the absence of features lower in energy than the ν_3 fundamental. For Fe_5O^- , the envelope of the FC simulation in Fig. 7(a) is an excellent qualitative match for our experimental results, confirming the preferential μ_2 structures of $\text{Fe}_5\text{O}^{0/-}$. Modes ν_5 , ν_7 , and ν_8 demonstrate significant FC intensity, while ν_1 , ν_3 , and ν_6 appear more weakly. All modes have somewhat exaggerated FC intensity in the simulation compared to experiment, and some calculated fundamental frequencies are higher than experimental frequencies. We plot FC simulations for photodetachment transitions of the alternative C_{1-} and C_s -symmetric μ_3 structures of $\text{Fe}_5\text{O}^{0/-}$ in Fig. S3;⁷⁴ both are comparatively very poor matches with the observed experimental structure.

Fitting the FC simulation parameters to the experimental overviews, as described in Section IV B, yields the simulations in Figs. 6(b) and 7(b) and the altered parameters for neutral Fe_4O and Fe_5O in the rightmost columns of Tables III and IV. In fitting the FC activity of totally symmetric modes to the experiment, we arrive at new values for the displacement between anion and neutral structures and, keeping the DFT anion geometries fixed, new neutral bond lengths. These fitted bond lengths represent a fairly minor update in geometry from the DFT results for both neutral clusters; the norm of the geometry difference between the DFT and neutral geometries is 0.04 Å for Fe_4O and 0.03 Å for Fe_5O . The corresponding change in the simulated spectra highlights the sensitivity of FC structure to small changes in displacement, particularly for the three-dimensional structures exhibited by metal oxide clusters.

The results of the FC simulation and fitting inform our interpretation of the high-resolution SEVI spectra; all vibrational frequencies observed experimentally are compared to their calculated values in Table V. In the Fe_4O^- spectrum (Fig. 2), we can unambiguously assign peak D at a shift of 236 cm^{-1} from the origin to 3_0^1 ; the ν_3 fundamental is calculated at 232-236 cm^{-1} . Peak E at 325 cm^{-1} is assigned to 2_0^1 . The ν_2 fundamental is calculated higher in frequency at 352-366 cm^{-1} , but falls within the error of DFT vibrational frequencies for species involving transition metals.⁶⁶ Peaks F, G, and H are the 3_0^2 , $2_0^1 3_0^1$, and 2_0^2 transitions respectively. The ν_1 fundamental, calculated to lie at 644-658 cm^{-1} , may also be underlying peak H, which lies 654 cm^{-1} above the vibrational origin. Mode ν_1 is not predicted to have much FC activity however, so we do not make an assignment.

At low binding energies, two closely spaced peaks B and C are resolved at respective shifts of 163 and 175 cm^{-1} above the Fe_4O^- vibrational origin. We assign peak C as 4_0^1 , as the ν_4 fundamental is calculated to lie at 169-175 cm^{-1} . Peak B does not align with the calculated frequency of any totally symmetric vibrational mode, but it could arise from a $\Delta\nu = 2$ transition in a non-totally symmetric mode. The only non-totally symmetric mode of the $^{15}A_2$ state that lies sufficiently low in energy for two quanta of excitation to match the position of peak B is ν_5 (mode shown schematically in Fig. S2(a)⁷⁴). As mentioned in Section V A, the $^{15}A_2$ state of neutral Fe_4O has a double-well vibrational potential along the

ν_5 normal coordinate, which can lead to enhanced FC activity in transitions involving even quanta of excitation in ν_5 .

FC factors for transitions to ν_5 vibrational states are calculated by treating this mode as an anharmonic oscillator. Single-point calculations were carried out scanning a one-dimensional slice of the vibrational potential along the ν_5 coordinate for the neutral $^{15}A_2$ state and the anionic $^{16}B_2$ state. These points were then fit to a 16th order polynomial for the neutral state and a 4th order polynomial for the anion, and a MATLAB script was used to numerically solve for the vibrational eigenenergies and wavefunctions. These results are shown in Fig. 9 using TPSS/6-311+G*. We find $2\nu_5 = 149 \text{ cm}^{-1}$ which compares well to the experimental shift of peak B at 163 cm^{-1} .

We use direct integration of the anion and neutral vibrational wavefunctions to solve for the Franck-Condon factors $|\langle v_{neutral} | v_{anion} \rangle|^2$ of the 5_0^n transitions. The calculated FC intensity of 5_0^2 relative to the vibrational origin is 0.12 using the TPSS functional; all other 5_0^n FC intensities are negligibly small. This value provides a good match with the experimental intensity of peak B, at about 10% of the origin intensity. We therefore assign peak B to the 5_0^2 transition.

Assigning the vibrational structure of the high-resolution Fe_5O^- SEVI spectrum in Fig. 3 is more straightforward. Three fundamentals can be assigned very clearly: peak B to the 8_0^1 transition, peak C to 7_0^1 , and peak D to 5_0^1 . Peaks F, G, and H then line up as $5_0^1 8_0^1$, $5_0^1 7_0^1$, and 5_0^2 . Peak E, lying 313 cm^{-1} from the vibrational origin, cannot be accounted for as part of a progression or a combination band, so it is likely the 3_0^1 fundamental, which is predicted to be FC active with calculated frequencies of 344-354 cm^{-1} . Peak I at 670 cm^{-1} is assigned to the 1_0^1 fundamental, which is calculated at 660-674 cm^{-1} and predicted to have similar FC intensity to what is observed experimentally.

The Franck-Condon structure of the main photodetachment bands of both clusters can also be rationalized in the context of the α HOMOs from which the electron is detached.

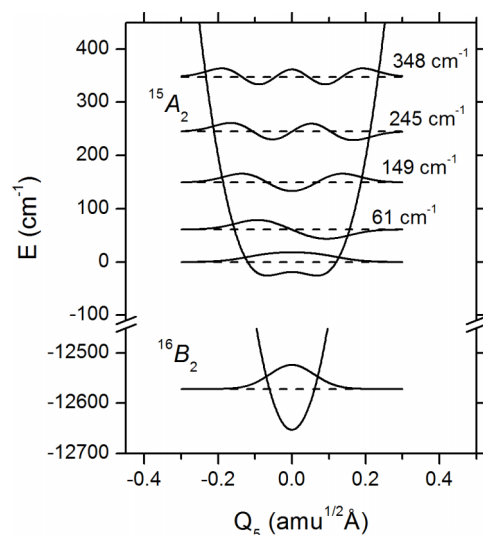


FIG. 9. Vibrational potential, low-lying eigenenergies, and wavefunctions for the ν_5 mode of the $^{16}B_2$ state of Fe_4O^- and the $^{15}A_2$ state of Fe_4O , calculated with TPSS/6-311+G*.

Both α HOMOs feature s -like lobes of opposite phase localized on the Fe(3) and Fe(4) atoms (Fig. 8). Accordingly, the bond between the Fe(3) and Fe(4) atoms shrinks upon photodetachment by 0.10 Å for Fe_4O^- and 0.11 Å for Fe_5O^- , consistent with removal of an electron from an antibonding orbital. The vibrational states of the neutral clusters that are populated after photodetachment correspondingly involve modes with significant distortion of the bond between the Fe(3) and Fe(4) atoms, where the primary change in the electron density occurs upon detachment.

VI. CONCLUSIONS

We report a high-resolution photoelectron imaging study of cryogenically cooled Fe_4O^- and Fe_5O^- iron monoxide cluster anions using SEVI spectroscopy. Our results represent the first vibrationally resolved spectra of these species, providing precise electron affinities and excited state term energies as well as newly observed and assigned vibrational frequencies. Through comparison of our experimental results with DFT calculations and Franck-Condon simulations, we determine the structural isomers and electronic states of these clusters. The experimental and theoretical results point to C_{2v} -symmetric $\text{Fe}_4\text{O}^{0/-}$ and C_s -symmetric $\text{Fe}_5\text{O}^{0/-}$ clusters, both of which preferentially bind the O atom in a μ_2 configuration.

This work represents the next step in our extension of the cryo-SEVI technique towards ever-larger transition metal oxide clusters. We demonstrate here that clusters involving four and five metal centers are accessible to detailed characterization with good agreement between spectroscopic and theoretical methods, despite the presence of multiple low-energy electronic states and structural isomers. In future work, it will be of considerable interest to study Fe_nO^- clusters complexed to small molecules such as CO as a model system for CO oxidation by iron oxide catalysts.

ACKNOWLEDGMENTS

This research is funded by the Air Force Office of Scientific Research under Grant No. FA9550-16-1-0097. M.L.W. thanks the National Science Foundation for a graduate research fellowship.

- ¹P. Li, D. E. Miser, S. Rabiei, R. T. Yadav, and M. R. Hajaligol, *Appl. Catal. B* **43**, 151 (2003).
- ²A. K. Kandalam, B. Chatterjee, S. N. Khanna, B. K. Rao, P. Jena, and B. V. Reddy, *Surf. Sci.* **601**, 4873 (2007).
- ³D. S. Newsome, *Cat. Rev.-Sci. Eng.* **21**, 275 (1980).
- ⁴C. Rhodes, G. J. Hutchings, and A. M. Ward, *Catal. Today* **23**, 43 (1995).
- ⁵L. G. Xu, S. Bao, R. J. O'Brien, D. J. Houpt, and B. H. Davis, *Fuel Sci. Technol. Int.* **12**, 1323 (1994).
- ⁶W. Weiss and W. Ranke, *Prog. Surf. Sci.* **70**, 1 (2002).
- ⁷V. Kesavan, D. Dhar, Y. Koltypin, N. Perkass, O. Palchik, A. Gedanken, and S. Chandrasekaran, *Pure Appl. Chem.* **73**, 85 (2001).
- ⁸M. M. Schubert, S. Hackenberg, A. C. van Veen, M. Muhler, V. Plzak, and R. J. Behm, *J. Catal.* **197**, 113 (2001).
- ⁹R. O. Ramabhadran, J. E. Mann, S. E. Waller, D. W. Rothgeb, C. C. Jarrold, and K. Raghavachari, *J. Am. Chem. Soc.* **135**, 17039 (2013).
- ¹⁰K. A. Zemski, D. R. Justes, and A. W. Castleman, *J. Phys. Chem. B* **106**, 6136 (2002).
- ¹¹D. K. Böhme and H. Schwarz, *Angew. Chem., Int. Ed.* **44**, 2336 (2005).
- ¹²M. J. Cheng, K. Chenoweth, J. Oxgaard, A. van Duin, and W. A. Goddard, *J. Phys. Chem. C* **111**, 5115 (2007).
- ¹³Y. D. Kim, *Int. J. Mass Spectrom.* **238**, 17 (2004).
- ¹⁴G. E. Johnson, R. Mitrić, V. Bonacić-Koutecký, and A. W. Castleman, *Chem. Phys. Lett.* **475**, 1 (2009).
- ¹⁵K. R. Asmis, *Phys. Chem. Chem. Phys.* **14**, 9270 (2012).
- ¹⁶B. V. Reddy and S. N. Khanna, *Phys. Rev. Lett.* **93**, 068301 (2004).
- ¹⁷H. Schwarz, *Int. J. Mass Spectrom.* **237**, 75 (2004).
- ¹⁸J. B. Kim, M. L. Weichman, and D. M. Neumark, *J. Chem. Phys.* **141**, 174307 (2014).
- ¹⁹J. B. Kim, M. L. Weichman, and D. M. Neumark, *J. Am. Chem. Soc.* **136**, 7159 (2014).
- ²⁰S. J. Riley, E. K. Parks, G. C. Nieman, L. G. Pobo, and S. Wexler, *J. Chem. Phys.* **80**, 1360 (1984).
- ²¹Q. Sun, M. Sakurai, Q. Wang, J. Z. Yu, G. H. Wang, K. Sumiyama, and Y. Kawazoe, *Phys. Rev. B* **62**, 8500 (2000).
- ²²D. N. Shin, Y. Matsuda, and E. R. Bernstein, *J. Chem. Phys.* **120**, 4150 (2004).
- ²³S. Yin, W. Xue, X.-L. Ding, W.-G. Wang, S.-G. He, and M.-F. Ge, *Int. J. Mass Spectrom.* **281**, 72 (2009).
- ²⁴K. S. Molek, C. Anfuso-Cleary, and M. A. Duncan, *J. Phys. Chem. A* **112**, 9238 (2008).
- ²⁵M. Li, S.-R. Liu, and P. B. Armentrout, *J. Chem. Phys.* **131**, 144310 (2009).
- ²⁶W. Xue, S. Yin, X.-L. Ding, S.-G. He, and M.-F. Ge, *J. Phys. Chem. A* **113**, 5302 (2009).
- ²⁷M. C. Oliveira, J. Marçalo, M. C. Vieira, and M. A. Almoester Ferreira, *Int. J. Mass Spectrom.* **185**, 825 (1999).
- ²⁸Y. Xie, F. Dong, S. Heimbuch, J. J. Rocca, and E. R. Bernstein, *J. Chem. Phys.* **130**, 114306 (2009).
- ²⁹N. M. Reilly, J. U. Reveles, G. E. Johnson, J. M. del Campo, S. N. Khanna, A. M. Koster, and A. W. Castleman, *J. Phys. Chem. C* **111**, 19086 (2007).
- ³⁰N. M. Reilly, J. U. Reveles, G. E. Johnson, S. N. Khanna, and A. W. Castleman, *J. Phys. Chem. A* **111**, 4158 (2007).
- ³¹W. Xue, Z.-C. Wang, S.-G. He, Y. Xie, and E. R. Bernstein, *J. Am. Chem. Soc.* **130**, 15879 (2008).
- ³²J. U. Reveles, G. E. Johnson, S. N. Khanna, and A. W. Castleman, *J. Phys. Chem. C* **114**, 5438 (2010).
- ³³H. Wu, S. R. Desai, and L.-S. Wang, *J. Am. Chem. Soc.* **118**, 5296 (1996).
- ³⁴G. V. Chertihin, W. Saffel, J. T. Yustein, L. Andrews, M. Neurock, A. Ricca, and C. W. Bauschlicher, *J. Phys. Chem.* **100**, 5261 (1996).
- ³⁵N. O. Jones, B. V. Reddy, F. Rasouli, and S. N. Khanna, *Phys. Rev. B* **72**, 165411 (2005).
- ³⁶S. López, A. H. Romero, J. Mejía-López, J. Mazo-Zuluaga, and J. Restrepo, *Phys. Rev. B* **80**, 085107 (2009).
- ³⁷X.-L. Ding, W. Xue, Y.-P. Ma, Z.-C. Wang, and S.-G. He, *J. Chem. Phys.* **130**, 014303 (2009).
- ³⁸B. F. Xu, C. L. Yang, M. S. Wang, and X. G. Ma, *Mol. Phys.* **109**, 1889 (2011).
- ³⁹P. C. Engelking and W. C. Lineberger, *J. Chem. Phys.* **66**, 5054 (1977).
- ⁴⁰A. S. C. Cheung, R. M. Gordon, and A. J. Merer, *J. Mol. Spectrosc.* **87**, 289 (1981).
- ⁴¹T. Andersen, K. R. Lykke, D. M. Neumark, and W. C. Lineberger, *J. Chem. Phys.* **86**, 1858 (1987).
- ⁴²A. J. Merer, *Annu. Rev. Phys. Chem.* **40**, 407 (1989).
- ⁴³Y. Gong, M. F. Zhou, and L. Andrews, *Chem. Rev.* **109**, 6765 (2009).
- ⁴⁴J. B. Kim, M. L. Weichman, and D. M. Neumark, *Mol. Phys.* **113**, 2105 (2015).
- ⁴⁵L. S. Wang, J. W. Fan, and L. Lou, *Surf. Rev. Lett.* **3**, 695 (1996).
- ⁴⁶G. L. Gutsev, C. W. Bauschlicher, H. J. Zhai, and L.-S. Wang, *J. Chem. Phys.* **119**, 11135 (2003).
- ⁴⁷D. M. Cox, D. J. Trevor, R. L. Whetten, E. A. Rohlfing, and A. Kaldor, *Phys. Rev. B* **32**, 7290 (1985).
- ⁴⁸G. L. Gutsev and C. W. Bauschlicher, *J. Phys. Chem. A* **107**, 7013 (2003).
- ⁴⁹H. Shiroishi, T. Oda, I. Hamada, and N. Fujima, *Eur. Phys. J. D* **24**, 85 (2003).
- ⁵⁰H. Shiroishi, T. Oda, I. Hamada, and N. Fujima, *Polyhedron* **24**, 16 (2005).
- ⁵¹A. Osterwalder, M. J. Nee, J. Zhou, and D. M. Neumark, *J. Chem. Phys.* **121**, 6317 (2004).
- ⁵²D. M. Neumark, *J. Phys. Chem. A* **112**, 13287 (2008).
- ⁵³C. Hock, J. B. Kim, M. L. Weichman, T. I. Yacovitch, and D. M. Neumark, *J. Chem. Phys.* **137**, 244201 (2012).
- ⁵⁴U. Even, J. Jortner, D. Noy, N. Lavie, and C. Cossart-Magos, *J. Chem. Phys.* **112**, 8068 (2000).
- ⁵⁵W. C. Wiley and I. H. McLaren, *Rev. Sci. Instrum.* **26**, 1150 (1955).
- ⁵⁶A. T. J. B. Eppink and D. H. Parker, *Rev. Sci. Instrum.* **68**, 3477 (1997).
- ⁵⁷D. W. Chandler and P. L. Houston, *J. Chem. Phys.* **87**, 1445 (1987).
- ⁵⁸M. L. Weichman, J. A. DeVine, D. S. Levine, J. B. Kim, and D. M. Neumark, *Proc. Natl. Acad. Sci. U. S. A.* **113**, 1698 (2016).

- ⁵⁹M. B. Doyle, C. Abeyasera, and A. G. Suits, NuACQ, <http://chem.wayne.edu/suitsgroup/NuACQ.html> (2012).
- ⁶⁰B. Dick, *Phys. Chem. Chem. Phys.* **16**, 570 (2014).
- ⁶¹C. Blondel, W. Chaibi, C. Delsart, C. Drag, F. Goldfarb, and S. Kroger, *Eur. Phys. J. D* **33**, 335 (2005).
- ⁶²A. Sanov and R. Mabbs, *Int. Rev. Phys. Chem.* **27**, 53 (2008).
- ⁶³J. B. Kim, M. L. Weichman, T. I. Yacovitch, C. Shih, and D. M. Neumark, *J. Chem. Phys.* **139**, 104301 (2013).
- ⁶⁴J. Cooper and R. N. Zare, *J. Chem. Phys.* **48**, 942 (1968).
- ⁶⁵B. Baguenard, J. C. Pinaré, C. Bordas, and M. Broyer, *Phys. Rev. A* **63**, 023204 (2001).
- ⁶⁶C. J. Cramer and D. G. Truhlar, *Phys. Chem. Chem. Phys.* **11**, 10757 (2009).
- ⁶⁷A. J. Wachtors, *J. Chem. Phys.* **52**, 1033 (1970).
- ⁶⁸P. J. Hay, *J. Chem. Phys.* **66**, 4377 (1977).
- ⁶⁹M. J. Frisch, G. W. Trucks, H. B. Schlegel, G. E. Scuseria, M. A. Robb, J. R. Cheeseman, G. Scalmani, V. Barone, B. Mennucci, G. A. Petersson, H. Nakatsuji, M. Caricato, X. Li, H. P. Hratchian, A. F. Izmaylov, J. Bloino, G. Zheng, J. L. Sonnenberg, M. Hada, M. Ehara, K. Toyota, R. Fukuda, J. Hasegawa, M. Ishida, T. Nakajima, Y. Honda, O. Kitao, H. Nakai, T. Vreven, J. A. Montgomery, J. E. Peralta, F. Ogliaro, M. Bearpark, J. J. Heyd, E. Brothers, K. N. Kudin, V. N. Staroverov, R. Kobayashi, J. Normand, K. Raghavachari, A. Rendell, J. C. Burant, S. S. Iyengar, J. Tomasi, M. Cossi, N. Rega, J. M. Millam, M. Klene, J. E. Knox, J. B. Cross, V. Bakken, C. Adamo, J. Jaramillo, R. Gomperts, R. E. Stratmann, O. Yazyev, A. J. Austin, R. Cammi, C. Pomelli, J. W. Ochterski, R. L. Martin, K. Morokuma, V. G. Zakrzewski, G. A. Voth, P. Salvador, J. J. Dannenberg, S. Dapprich, A. D. Daniels, Ö. Farkas, J. B. Foresman, J. V. Ortiz, J. Cioslowski, and D. J. Fox, GAUSSIAN 09, Revision C.01, 2011 <http://www.gaussian.com>.
- ⁷⁰K. M. Ervin, PESCAL, <http://wolfweb.unr.edu/~ervin/pes> (2010).
- ⁷¹K. M. Ervin, T. M. Ramond, G. E. Davico, R. L. Schwartz, S. M. Casey, and W. C. Lineberger, *J. Phys. Chem. A* **105**, 10822 (2001).
- ⁷²F. Duschinsky, *Acta Physicochim. URSS* **7**, 551 (1937).
- ⁷³R. Mabbs, E. R. Grumbling, K. Pichugin, and A. Sanov, *Chem. Soc. Rev.* **38**, 2169 (2009).
- ⁷⁴See supplementary material at <http://dx.doi.org/10.1063/1.4960176> for details of calculated electronic states, energetics, geometries and vibrational frequencies, spectrum showing thermionic emission from Fe₅O⁻, visualization of Franck-Condon active vibrational normal modes, and Franck-Condon simulations for alternate structures of Fe₅O^{0/-}.